$\lambda = 2.4 - 5\,\mu$m spectroscopy with the JWST NIRCam instrument

Thomas P. Greene[a,*], Douglas M. Kelly[b], John Stansberry[c], Jarron Leisenring[b], Eiichi Egami[b], Everett Schlawin[b], Laurie Chu[d], Klaus W. Hodapp[d], Marcia Rieke[b]
[a]NASA Ames Research Center, Moffett Field, CA, USA, 94035
[b]Steward Observatory, University of Arizona, Tucson, AZ, USA, 85721
[c]Space Telescope Science Institute, Baltimore, MD, USA, 21218
[d]Institute for Astronomy, University of Hawai'i, Hilo, HI, USA, 96720

Abstract. The James Webb Space Telescope near-infrared camera (JWST NIRCam) has two $2\rlap{.}'2 \times 2\rlap{.}'2$ fields of view that can be observed with either imaging or spectroscopic modes. Either of two $R \sim 1500$ grisms with orthogonal dispersion directions can be used for slitless spectroscopy over $\lambda = 2.4 - 5.0\,\mu$m in each module, and shorter wavelength observations of the same fields can be obtained simultaneously. We describe the design drivers and parameters of the grisms and present the latest predicted spectroscopic sensitivities, saturation limits, resolving powers, and wavelength coverage values. Simultaneous short wavelength ($0.6 - 2.3\,\mu$m) imaging observations of the $2.4 - 5.0\,\mu$m spectroscopic field can be performed in one of several different filter bands, either in-focus or defocused via weak lenses internal to NIRCam. The grisms are available for single-object time series spectroscopy and wide-field multi-object slitless spectroscopy modes in the first cycle of JWST observations. We present and discuss operational considerations including subarray sizes and data volume limits. Potential scientific uses of the grisms are illustrated with simulated observations of deep extragalactic fields, dark clouds, and transiting exoplanets. Information needed to plan observations using these spectroscopic modes are also provided.

Keywords: infrared spectroscopy, satellites, space optics, gratings, cameras.

*Tom Greene, tom.greene@nasa.gov

1 Introduction

The near-infrared camera (NIRCam) of the James Webb Space Telescope (JWST) has flexible modes that provide wide-field imaging through narrow-, medium- or wide-band filters, coronagraphic imaging, and slitless spectroscopy.[1–5] Long-wavelength (LW; $\lambda = 2.4 - 5.0\,\mu$m) Si grisms[6] and $\lambda = 1 - 2\,\mu$m Dispersed Hartmann Sensors (DHSs) were developed for the purposes of wavefront sensing and telescope primary segment phasing with NIRCam.[7] The DHSs provide $R \equiv \lambda/\delta\lambda \simeq 300$ spectra of bright point sources.[8] The LW grisms have been approved and are being supported for scientific use in Cycle 1 and later, and the DHSs are being considered for scientific use after Cycle 1.

The NIRCam instrument is composed of two nearly identical optical modules (A and B), each having a $2\rlap{.}'2 \times 2\rlap{.}'2$ field of view (FOV). Wavelengths $\lambda < 2.4\,\mu$m are imaged by the short-wavelength (SW) channel of each module which has a focal plane of four abutted 2048×2048 (2040×2040 active) pixel HAWAII-2RG detectors with a plate scale of 32 mas pixel^{-1}. A dichroic beamsplitter sends longer wavelengths to the LW channel that has a single 2048×2048 (2040×2040 active) pixel HAWAII-2RG detector focal plane with a plate scale of 65 mas pixel^{-1}.[1,3] This allows simultaneous SW and LW imaging of the same NIRCam field with each module. The pupil wheels in the LW channels of each module are equipped with two identical Si grisms with perpendicular orientations so that light is dispersed along either the rows (R grisms) of columns (C grisms) of their detectors. The NIRCam pupil wheels are located at actual pupils and are in series with filter wheels. Therefore the grisms must be used in series with a filter wheel element. The chosen filter wheel element (filter) selects the wavelength range desired for each observation and

rejects unwanted spectral orders. Each module also has two SW pupil wheel positions containing a DHS for SW spectroscopy.

This article will focus on the LW grisms since DHS performance and scientific applications have recently been described in Ref. 8. The following section describes the grism design drivers and adopted design. Their spectroscopic capabilities and expected performance in NIRCam are presented next. That is followed by sections on planned spectroscopic operations and sample observation simulations. The paper concludes with a section on observation planning and available tools.

2 Grism Design

The grism design was driven by JWST coarse phasing wavefront sensing requirements for achieving maximum segment piston capture range and good resolution of segment piston positions (small minimum detectable piston). The grisms would be used as dispersed fringe sensors (DFSs) in order to measure segment piston errors.[7] The large capture range requirement drives the design toward producing spectra at the longest possible wavelengths, and a small minimum detectable piston drives the design toward larger spectral coverage. These effects are coupled for a fixed long-wavelength cutoff: large spectral ranges provide small minimum detectable pistons, but their relatively small short wavelength limits reduce the maximum piston capture range. The instantaneous spectral coverage of an observation is set by spectral dispersion and limited by finite detector size and the free spectral range of the spectral order used.

These factors drove the long wavelength grism effective cutoff to be set to NIRCam's long wavelength detector and filter cutoff, $\lambda = 5.0$ μm. The adopted design sets spectral dispersion to be 10.0 Å pixel^{-1}, producing a central undeviated wavelength $\lambda = 4.0$ μm and a short wavelength cutoff $\lambda = 3.0$ μm on NIRCam's LW detector arrays. These nominal wavelength cutoffs apply when a source is located at the center of the field of view. This large operating wavelength range dictates that the grisms operate in first order, m = 1.

Equation (5) of Ref. 9 shows that the maximum detectable wavefront piston error of a grism used as a DFS is $\delta L_{\max} \propto R_0 \lambda_B^2$ where R_0 is the effective spectral resolving power and λ_B is the blue (short wavelength) cutoff of the filter used with the grism. Long-wavelength filters have large λ_B and therefore have large capture ranges. The effective resolving power of a grism used to phase two adjacent primary mirror segments is $R_0 = mN_0$ where N_0 is the number of grism grooves that span the distance between the 2 segment centers, $\simeq 0.2\times$ the total number of grooves that span the pupil. Using the NIRCam grism groove frequency 65 mm^{-1} (Table 1), the 31 mm pupil diameter,[10] and $\lambda_B = 3.88$ μm, then the F444W filter (Table 4) gives maximum detectable piston of $\simeq \pm 200\mu$m, where this physical distance is 1/2 of the optical $\delta L_{\max}$ from Eqn. (5) of Ref. 9. Errors larger than this maximum piston can be detected directly from the telescope point spread function. The minimum detectable wavefront piston error is set by the smallest measurable displacement between the red and blue ends of fringes. This can be evaluated by computing the cross-dispersion centroid locations of the fringes at the long and short wavelength ends of a given filter bandpass. If the measurement precision of the fringe profile centroid is 0.05 pixel, then the minimum detectable piston is ± 0.12 μm using the F444W and F322W2 filters.[11,12] The telescope segments are now expected to always be within the capture range of the DHS measurements, so the grisms will likely be only used for science applications and not for wavefront sensing.

Table 1 Basic grism parameters.

Material	Optical grade mono-crystalline Si
Operating temperature	$\sim 30 - 35$ K
Groove frequency	65 mm^{-1}
Prism angle	6.16°
Blaze angle	5.75°
Maximum thickness	8.0 mm
Diameter	48.0 mm, circular with side flats
Clear Aperture	42.0 mm, circular
AR coating	2.4 - 5.0 μm

Several practical issues also drove the grism design. First, the NIRCam pupil and filter wheels are spaced closely, separated by only about 10 mm. The elements in these wheels are also large, with 48 mm diameters and 42 mm clear apertures. This requires the grism to have a small prism angle, less than about 10 degrees. Given this small angle, the relatively high dispersion (10.0 Å pixel^{-1}) dictates a high refractive index, $n \gtrsim 2.5$, as derived from standard first-order grism design equations.[13,14] The grism material must also maintain high and uniform optical transmission after exposure to a significant dose of cosmic radiation over the lifetime of JWST. The radiation at JWST's L2 orbit location will be dominated by high energy α particles, and we estimate that the total ionizing dose experienced by the grisms will be less than ~ 10 krad(Si) for a 10 year mission. This was determined from the 10 year $JWST$ mission dose[15] after adjusting for the expected 2018 launch date (near solar minimum) and the ~ 2 mm of Ti shielding the grisms. We selected mono-crystalline Si as the grism material given its infrared transmission, high refractive index (n = 3.4 at T= 35K[16]), and high radiation tolerance.[17]

The blaze angle was chosen to maximize efficiency near $\lambda = 3.7\mu$m, the mean wavelength of the $\lambda = 2.4 - 5.0$ μm LW modules. This is slightly different from the undeviated wavelength ($\lambda = 4.0\mu$m), so the blaze angle is offset slightly from the prism angle. The basic manufacturing specifications of the grisms are given in Table 1. The grisms were fabricated via micro-lithographic etching techniques at the University of Texas at Austin[6] and were anti-reflection (AR) coated by II–VI Infrared. All four flight grisms were coated on their flat faces, and two were coated on their grooved faces. Two were left uncoated on their grooved sides as a precautionary measure in case there were adhesion problems or coating non-uniformities due to the grooves. However, no such problems have been identified after several cryogenic cycles. The two grisms that were coated on both faces are located in NIRCam Module A, while the grisms that were coated only on their flat ungrooved faces are located in Module B. The dispersions of all four grisms were measured to be within 1% of the 10.0 Å pixel^{-1} design value during JWST science instrument testing at NASA Goddard Space Flight Center (GSFC) during the summer of 2014.
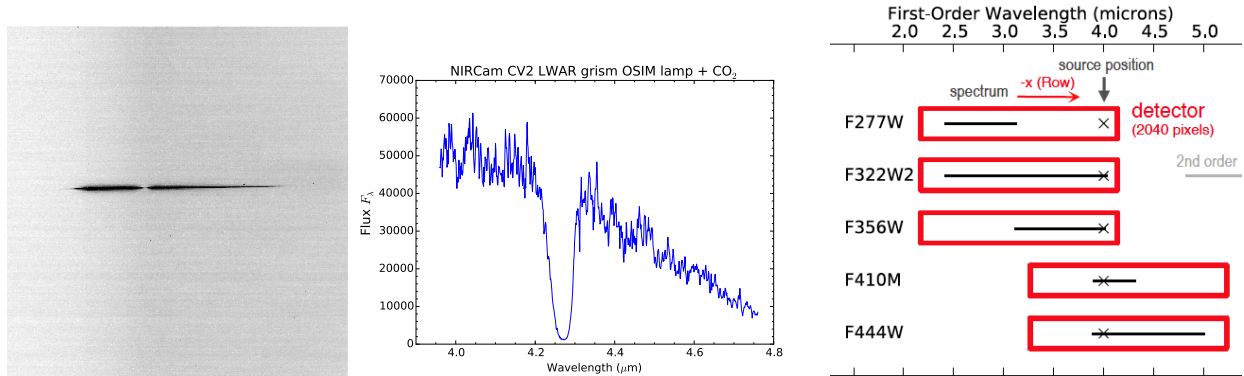
Fig 1 Left: NIRCam spectral image of the OSIM super-continuum lamp taken with the LWA R grism and F444W filter during JWST instrument instrument testing at NASA GSFC in August 2014. The image is oriented so that detector x coordinates increase to the left and wavelength increases to the right. Center: Extracted spectrum from the image with an approximate wavelength calibration applied. The continuum decreases toward longer wavelengths due to low fiber transmittance, and the broad feature near 4.27 μm is due to CO_2 absorption. Both of these features are artifacts of the test equipment and not NIRCam itself. Right: Layout of an object's LW R grism spectra spectrum relative to its direct image position for different filters (image courtesy of D. Coe).

3 Grism Spectroscopic Capabilities

3.1 Grism Usage

Filters are used in series with grisms to select the spectral bandpass desired for each observation. The NIRCam LW filter wheel contains filters that have medium ($\lambda/\Delta\lambda \sim 8 - 20$), wide ($\lambda/\Delta\lambda \sim 4 - 5$), and extra-wide ($\lambda/\Delta\lambda \sim 1 - 2$) bandpasses, and any of these can be used with the grisms in principle.[18] A subset of these is being defined for science applications. All LW narrow-band filters reside in the same pupil wheel as the grisms, so these cannot be used in series with the grisms. Each grism spans the entire pupil (image of the telescope primary), and any source in the NIRCam imaging field will have its light dispersed by a grism that is selected in the pupil wheel. Some of the dispersed spectrum may land outside of the FOV and not be recorded by the detector depending on the object field position and the selected filter (see Sec. 4). Spectra of sources slightly outside (to $\sim$10% beyond the field size) of the imaging field of view can be recorded by the detectors. The image and extracted spectrum of a NIRCam Module A LW grism exposure taken during the JWST instrument test campaign at NASA GSFC in 2014 is shown in Fig. 1. This figure also shows the layout of an object's LW R grism spectra spectra relative to its direct image position for different filters.

The grisms are usually operated in first order (m = 1), where they have maximum efficiency in NIRCam's LW bandpass. Their high dispersions, the finite size of the NIRCam field and detectors, and the limited bandpasses of the series filters all limit the detection of other orders. It is only possible to detect m $\neq$ 1 light when using the F322W2 filter with an LW grism. In that case, an object at the right location can produce a spectrum that is m = 1 at long wavelengths and m = 2 at short wavelengths within the F322W2 bandpass (see Fig. 1 right panel).

4

3.2 Resolving Power, Sensitivities, and Saturation Limits

The transmittance and reflectance values of all NIRCam optical components used for imaging observations have been measured from actual parts or test samples. The composite throughput values for Module A including the optical telescope element (OTE) reflectivity as well as NIRCam detector quantum efficiency are shown in Fig. 2. This figure also shows the theoretical first-order Module A and B LW grism efficiencies and Module B grism measurements at two wavelengths near 3 μm made during pre-delivery instrument testing at the Lockheed Martin Advanced Technology Center in 2012 December. The grism efficiency must be multiplied by the NIRCam + OTE curve for the chosen series filter to produce the total system throughput at each wavelength (not shown). Module A LW grisms are AR coated on both sides, while those in the B module are coated only on their flat (non-grooved) sides. Therefore the Module B LW grism efficiencies are ~ 0.74 times that of the Module A ones, and the Module B ones produce some ghosts of bright spectra.

All NIRCam spectroscopy is conducted without using slits or other focal plane apertures, so the spectral resolving power R of its grism observations are determined by the dispersion, wavelength, its pupil shape,[19] detector sampling, and object size. We now incorporate these into the equation for spectral resolving power, $R \equiv \lambda/\Delta\lambda$. At wavelength λ, the point source spectral resolution is $\Delta\lambda = FWHM \times \delta\lambda$ where $FWHM$ is the full width at half maximum of the monochromatic point spread function (PSF) as sampled in NIRCam LW pixels, and $\delta\lambda$ is the spectroscopic dispersion, 10.0 Å pixel^{-1} (see Sec. 2). This dictates that R increases near linearly with wavelength at $\lambda \lesssim 4\ \mu$m where the under-sampled PSF is $\sim$2 pixels, then R increases less steeply at $\lambda \gtrsim 4\ \mu$m where diffraction increases the size of the NIRCam PSF, causing point sources to subtend more pixels. The quasi-hexagonal JWST pupil causes some light to be diffracted by fewer grism grooves than the maximum number that span the pupil ($N_{\max} = 31$ mm pupil$^{10} \times 65$ grooves mm^{-1}), reducing the maximum resolving power. This effect causes a 15% increase in the spectral PSF width of a circular pupil and a corresponding reciprocal loss in resolving power.[19] We estimate that the quasi-hexagonal JWST pupil causes a similar increase in the spectral PSF width over the spatial PSF, reducing the maximum resolving power to $R_{\max} \simeq 0.9 m N_{\max}$. We have incorporated this beam factor into our resolving power calculations by scaling the simulated, high resolution monochromatic PSF by a factor of 1.1 in the spectral dimension before sampling by the NIRCam pixels and computing the $FWHM$ in the equation for R above. The resultant spectroscopic resolving power for LW grism observations of point sources is shown in the right panel of Fig. 2. This can also be approximated with the function $R \simeq 3.35(\lambda/\mu\text{m})^4 - 41.9(\lambda/\mu\text{m})^3 + 95.5(\lambda/\mu\text{m})^2 + 536(\lambda/\mu\text{m}) - 240$ to within a few percent. The pixel-limited resolving power (strongest at $\lambda \lesssim 4\ \mu$m) may be improved with dithering of multiple observations.

Tables 2 and 3 give the 10 σ point-source continuum sensitivities for the Module A and B grisms using a 2 spectral $\times$ 5 spatial pixel extraction aperture in 10^4 s of integration time. Unresolved point source emission line sensitivities are also given, using the spectral resolving power computed for each wavelength (right panel of Fig. 2). All sensitivities were calculated for estimated average zodiacal background levels using either the F322W2 or F444W filter in series, as identified in the table. These sensitivities are a factor of $\sim 2-3$ worse than expected for the JWST NIRSpec instrument, but NIRSpec cannot be operated in a true slitless mode.[20] Both NIRCam and the NIRSpec micro-shutter array (MSA) have similar fields of view. Lower background conditions than those assumed here will give sensitivities that are up to a factor of ~ 1.4 lower (better), and higher background conditions will result in sensitivities that are up to a factor of ~ 2
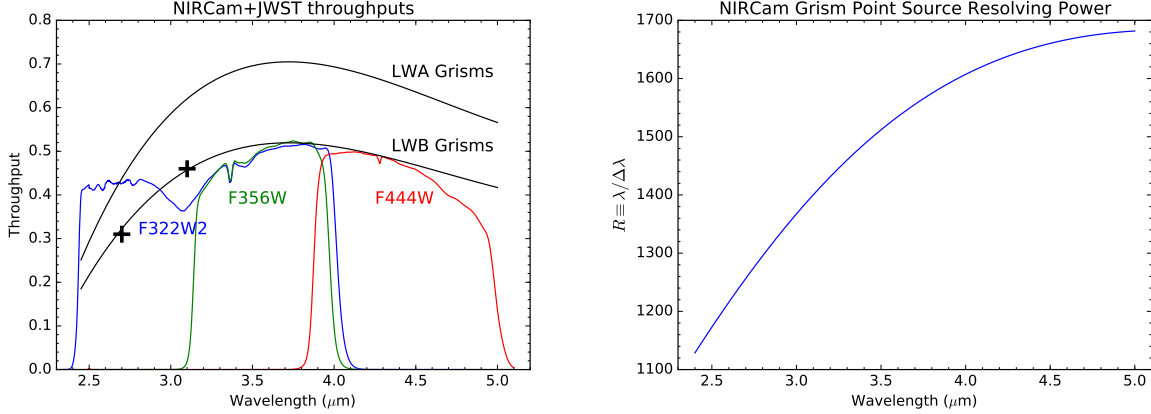
Fig 2 Left: Total system throughput including all OTE and NIRCam optics and the detector quantum efficiency for several NIRCam filters (Module A optics and QE shown; Module B is similar). The theoretical LW grism efficiency curves must be multiplied by the optics curves for a chosen filter to produce the system throughput at each wavelength. The Module B LW grisms are anti-reflection coated on only one side and therefore have throughputs approximately 25% lower than the LWA grisms. Module B grism throughputs were measured at 2 wavelengths and are shown as crosses. Right: Spline curve fit to the grism FWHM spectral resolving power R vs. wavelength for point sources. This is limited by pixel sampling of the PSF at shorter wavelengths ($\lambda \lesssim 4~\mu$m) and limited by diffraction and the quasi-hexagonal pupil shape[19] at longer wavelengths ($\lambda \gtrsim 4~\mu$m).

higher (worse). Using narrower band filters (i.e., F356W instead of F322W2, or F410M instead of F444W) can improve sensitivities by a factor of $\sim 1.2 - 2$. We also show the point-source continuum and emission-line sensitivities for F322W2, F410M, and F444W filters in Fig. 3. Tables 2 and 3 also give saturation values for 0.68 s integrations, 2 frame times for 2048×64 pixel subarrays with the detector operated using four outputs (stripe mode). Larger subarray stripes ($2048 \times >64$ pixels) will result in fainter bright limits, and operating in window mode (using a single detector output) will make the bright limits 1.5 mag fainter. The Module B grisms (Table 3) provide slightly larger (worse) sensitivities and brighter saturation limits than the Module A ones (Table 2) because the Module B grisms are AR coated on only one side and there are slight differences in the optical transmissions and detector quantum efficiencies between the modules.

4 Spectroscopic Operations

The NIRCam LW grisms are expected to be used in either of two modes: single-object time-series slitless spectroscopy or wide-field (multi-object) slitless spectroscopy. The layout of the grism dispersions on the NIRCam LW detectors and in the JWST focal plane is shown in Fig. 4. A single object can be positioned at the appropriate point to have its entire spectrum (as limited by the chosen filter) fall onto the detector array. Spectra of multiple objects in the imaging field will be recorded, and large sky areas can be mapped with multiple telescope pointings. The grisms can be operated in series with any filter in the NIRCam LW pupil wheel in principle, and the numerous choices allow optimization for spectral coverage, confusion, or sensitivity. Table 4 lists all wide and some of the medium-band the filters that will be enabled for use with the grisms during JWST observing Cycle 1. We expect those to be most popular, and the remaining medium-band

Table 2 Module A LW grism performance (F322W2 and F444W filters).

λ (μm)	F_{cont} (μ Jy)[a]	F_{line} (erg s^{-1} cm^{-2})[b]	K_{sat} (A0V)[c]	K_{sat} (M2V)[c]	Filter[d]
2.5	9.1	9.7E-18	4.3	4.2	F322W2
2.7	6.8	6.3E-18	4.4	4.4	F322W2
2.9	6.1	5.0E-18	4.3	4.3	F322W2
3.1	6.6	4.8E-18	4.1	4.1	F322W2
3.3	5.3	3.5E-18	4.1	4.3	F322W2
3.5	5.2	3.2E-18	4.0	4.2	F322W2
3.7	5.1	2.9E-18	3.9	4.1	F322W2
3.9	5.6	3.0E-18	3.7	3.9	F322W2
4.1	7.8	4.0E-18	3.4	3.7	F444W
4.3	8.7	4.3E-18	3.1	3.4	F444W
4.5	10	4.8E-18	2.9	3.0	F444W
4.7	13	5.9E-18	2.5	2.7	F444W
4.9	17	7.5E-18	2.1	2.4	F444W

[a] 10 σ point-source continuum sensitivities for 10,000 s integrations using a 2 (spectral) $\times$ 5 (spatial) pixel extraction aperture.

[b] 10 σ point-source unresolved emission line sensitivities for 10,000 s integrations using the actual FWHM PSF size and consequent spectral resolving power at this wavelength (right panel of Fig. 2).

[c] K-band Vega magnitudes for saturation (80% full well or 65,000 electrons) for 0.68 s integrations (2 reads) of 2048 $\times$ 64 pixel regions in stripe mode (4 outputs). Larger subarrays or use of only 1 output will result in fainter bright limits.

[d] Narrower filters will have similar saturation values and somewhat smaller (better) sensitivities.

LW filters (F250M, F300M, F335M, F360M, F410M, F480M) will also be available for use in wide-field mode in Cycle 1 and later.

The relatively high dispersion of the grisms cause spectra at extreme wavelengths (i.e., $\lambda <$ 3 μm and $\lambda \sim 5$ μm) to be displaced significantly ($\sim$1024 pixels or more) from the image location of the observed object in the dispersion direction. This means that wide-field grism observations taken with filters operating at extreme wavelengths will observe objects in an area considerably smaller than the full imaging field. For example, spectra taken with the F277W filter will fill only about half of the detector area. The missing spectra in the unfilled area would have object images outside of the NIRCam imaging field of view (see also Sec. 3.1). Objects further than $\sim$ 10% outside of the imaging field do not illuminate the NIRCam pick-off mirror (POM) and therefore cannot be observed.

The NIRCam detectors will be operated in their normal MULTIACCUM modes[21–23] during spectroscopic observations. High-precision time-series grism observations of bright objects (e.g., host stars of transiting planets) will likely require using a limited detector region to prevent saturation. Subarrays consisting of 64, 128, 256, or the full 2048 (including reference pixel) detector rows will be supported for single-object time-series LW grism observations. These can be read out either using all 4 outputs (stripe mode; spanning all 2048 columns) or else in window mode using a single output and possibly a smaller number of columns. Using the combination of stripe mode

Table 3 Module B LW grism performance (F322W2 and F444W filters).

λ (μm)	F_{cont} (μ Jy)[a]	F_{line} (erg s^{-1} cm^{-2})[b]	K_{sat} (A0V)[c]	K_{sat} (M2V)[c]	Filter[d]
2.5	11	1.2E-17	3.8	3.8	F322W2
2.7	8.6	7.9E-18	4.0	3.9	F322W2
2.9	7.7	6.2E-18	3.9	3.9	F322W2
3.1	8.2	5.9E-18	3.7	3.7	F322W2
3.3	6.5	4.3E-18	3.8	3.9	F322W2
3.5	6.2	3.8E-18	3.6	3.9	F322W2
3.7	6.0	3.4E-18	3.6	3.8	F322W2
3.9	6.3	3.3E-18	3.4	3.6	F322W2
4.1	9.5	4.8E-18	3.1	3.4	F444W
4.3	10	5.0E-18	2.9	3.2	F444W
4.5	12	5.4E-18	2.7	2.8	F444W
4.7	14	6.3E-18	2.3	2.6	F444W
4.9	17	7.4E-18	2.0	2.3	F444W

[a] 10 σ point-source continuum sensitivities for 10,000 s integrations using a 2 (spectral) $\times$ 5 (spatial) pixel extraction aperture.

[b] 10 σ point-source unresolved emission line sensitivities for 10,000 s integrations using the actual FWHM PSF size and consequent spectral resolving power at this wavelength (right panel of Fig. 2).

[c] K-band Vega magnitudes for saturation (80% full well or 65,000 electrons) for 0.68 s integrations (2 reads) of 2048 $\times$ 64 pixel regions in stripe mode (4 outputs). Larger subarrays or use of only 1 output will result in fainter bright limits.

[d] Narrower filters will have similar saturation values and somewhat smaller (better) sensitivities.

Table 4 Popular filters available for use with LW grisms

Filter Name[a]	λ_1 (μm)[b]	λ_2 (μm)[c]	# dispersed pixels	# pixels/2040[d]	Mode[e]
F277W	2.416	3.127	711	0.35	TS + WF
F322W2	2.430	4.013	1583	0.77	TS + WF
F356W	3.140	3.980	840	0.41	TS + WF
F444W	3.880	4.986	1106	0.54	TS + WF
F430M	4.167	4.398	231	0.11	WF
F460M	4.515	4.747	232	0.11	WF

[a] All LW M filters will also be available in wide-field mode; F430M and F460M are expected to be popular and are included for illustrative purposes
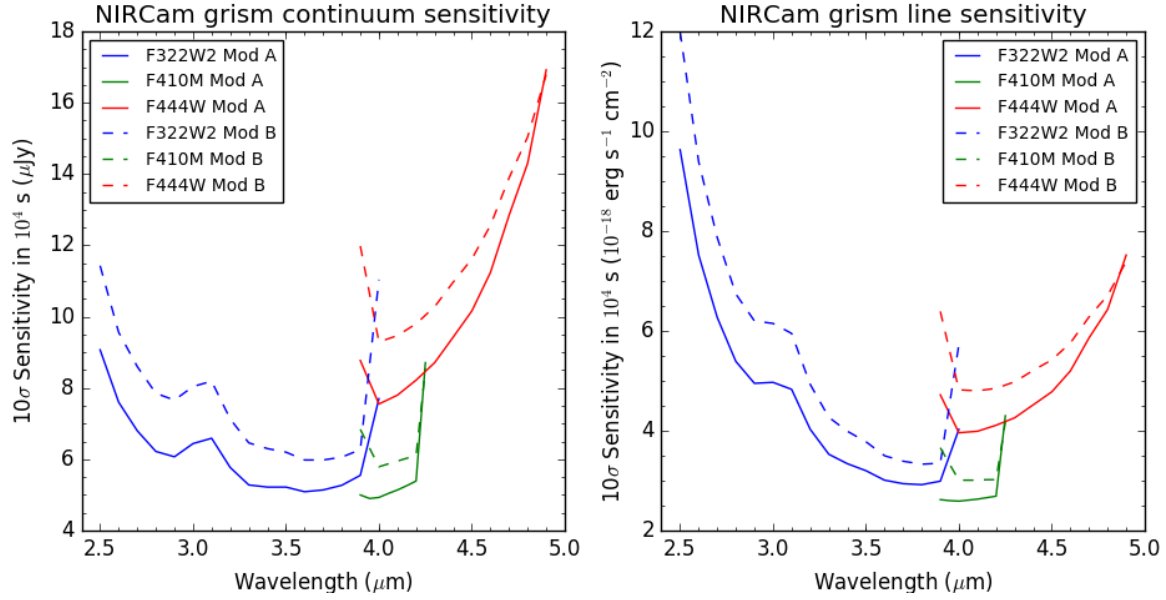
[b] Half-power wavelength (blue side)

[c] Half-power wavelength (red side)

[d] Fraction of the detector that a continuum spectrum occupies in the dispersion direction

[e] TS = single-object time series and WF = wide field modes

Fig 3 Point-source continuum (left) and emission line (right) sensitivities are shown for grisms with F322W2, F410M, and F444W filters for both Modules A and B. Note that the narrower bandwidth of the F410 filters results in significantly better sensitivity than the wider F444W at common wavelengths.
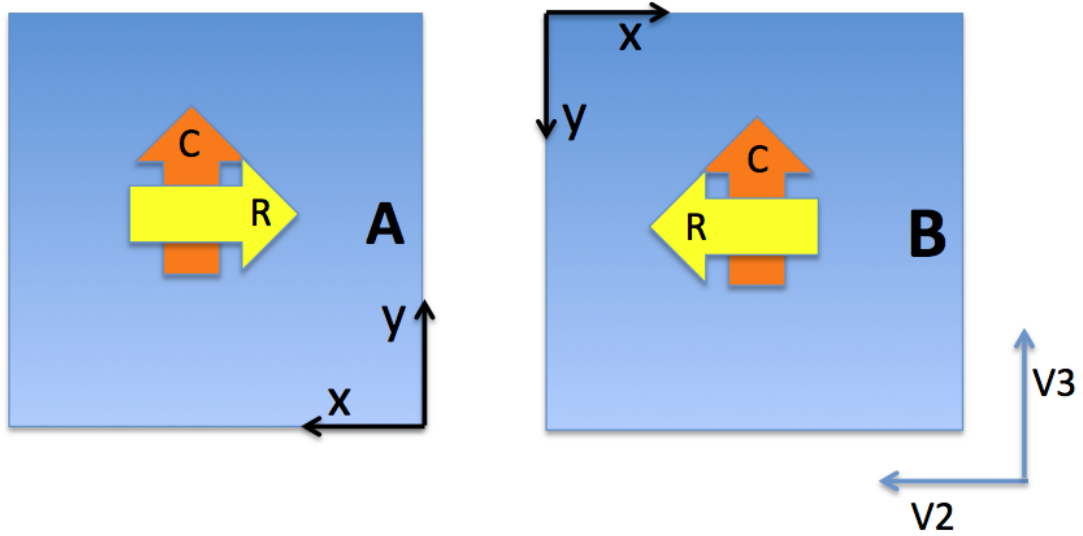
Fig 4 Grism dispersion orientations along detector axes (x, y) and the JWST observatory axes (V2, V3). The V3 position angle is defined to be 0 degrees when V2 points toward East and V3 points North on the sky. The yellow and orange arrows point in the direction of increasing wavelength for R and C grisms respectively in modules A (left) and B (right). Each module has a $2.'2 \times 2.'2$ imaging field of view.

9

and 64 detector rows gives the fastest readout time and provides the best bright limits (see Sec. 3.2, Table 2, and Table 3).

LW grism spectral observations can be partnered with simultaneous imaging observations of the same field in the SW channels. SW imaging observations can be conducted in-focus using only filters (in both LW spectroscopic modes), or else out of focus using a weak lens with a filter in series (single-object time-series mode only). Given the flux differences between dispersed spectra and in-focus images, we expect that many single-object point source observers will opt for using a weak lens in series with a filter in the SW channel for simultaneous observations with the LW grisms. It may be possible to obtain SW $\lambda = 1 - 2$ μm DHS spectra simultaneously with LW grism spectra if and when the DHSs are supported for scientific use.[8]

All NIRCam detectors will be operated with the same readout pattern and subarray size, so SW observations will use the same size detector region (full frame or subarray) as used for the LW grisms. At least 96% of the light from a point source using weak lens WLP8 (8 waves of defocus at 2.12 μm) in the SW channel will fall within a 2048 $\times$ 128 pixel subarray aperture. While the SW and LW subarrays have the same dimensions, their locations on the detectors can be individually specified. Tailoring of the SW and LW subarray positions is necessary because the SW pixel scale (32 mas pixel^{-1}; see Sec. 1) is ~half that of the LW channel. This causes the image of an object to fall at substantially different detector positions on the SW and LW detectors. The SW image can appear on different SW detectors, depending on where the source is in the LW field. When SW imaging or DHS data are taken in parallel with the LW grism data, particular care must be exercised to ensure that the single set of exposure parameters provide adequate dynamic range in both the SW and LW channels.

Most single-object time-series integrations will likely use the RAPID (every frame sample saved) or BRIGHT1 (every other frame sample saved) MULTIACCUM detector operation modes. This will produce a large amount of data, especially when conducting simultaneous SW and LW grism observations since they will use two (LW grism + SW imaging) or three detector arrays (LW grism + DHS if DHS use is implemented). The on-board solid state data recorder (SSR) can store 7 – 10 hours of RAPID data for 3 detector arrays operated in stripe mode (four outputs), and 28 – 40 hours of data when the detectors are operated with single outputs. JWST is expected to download data every 12 hours, so all but the longest transits of the brightest stars can be observed with both a LW grism and a SW element without overfilling the SSR.

5 Simulations of Spectroscopic Observations

We have developed software tools to simulate NIRCam spectroscopic LW grism observations in order to assess expected performance and to plan using NIRCam in both single-object and multi-object wide-field slitless spectroscopy modes. We describe these tools and present some results in this section.

The first simulator is designed to produce spectral images from multiple objects distributed in 2 spatial dimensions within a given NIRCam field. We have implemented this using the aXeSIM package, first developed for simulating HST WFC3 slitless spectroscopic images.[24] Spectra of individual objects can be extracted from simulated images using the companion aXe package[25] or other conventional astronomical data tools. We have produced aXeSIM configuration files that produce the expected signal and noise performance of the NIRCam LW grisms as we expect them to be used on JWST. In addition to producing the wide-field slitless spectroscopy simulations

in this section, we have used aXeSIM to validate the NIRCam performance estimates given in Table 2. aXeSIM-derived estimates agree within $\sim 10\%$ of pyNRC, the internal NIRCam team exposure time calculator.[26] The corresponding author of this publication will provide a package of the NIRCam LWA R grism configuration files for use with aXeSIM upon request. The recently released JWST exposure time calculator (ETC) can also be used to simulate and plan wide-field slitless spectroscopy observations (see Sec. 6).[27]

We have also developed a second simulator that is used to estimate the signals and noise expected for high precision time series observations of transiting planet spectra. These codes include the same throughputs (e.g., Fig. 2) used in the aXeSIM configuration files, and they also include an expected systematic noise floor in addition to the regular noise terms for detector read noise, dark noise, and observatory background noise components. One-dimensional simulations of exoplanet transmission (in transit) or emission (in secondary eclipse) spectra are produced, and they are described further in Ref. 28. The PandExo[29] transiting exoplanet tool can also be used to simulate and plan spectroscopic observations of transiting planets (see Sec. 6).

5.1 Wide-Field Slitless Spectroscopy of Extragalactic Fields

JWST is expected to revolutionize the study of high-redshift galaxies, allowing spectroscopic study of familiar rest-frame optical emission lines at high redshifts. With a wavelength coverage of $2.4 - 5$ μm, the NIRCam LW grism mode can detect Hα at $z = 2.7 - 6.6$, [O III] 5007 Å at $z = 3.8 - 9.0$, and [O II] 3727 Å at $z = 5.4 - 12.4$. Although NIRSpec will be the preferred choice for most extragalactic spectroscopic observations because of its superior sensitivity and wider wavelength coverage ($1 - 5$ μm for $R = 1000/2700$; $0.7 - 5.0$ μm for $R = 100$), the NIRCam LW grism mode does offer some interesting and potentially powerful capabilities. For example, the NIRCam LW grism mode will allow: (1) blind searches for strong line emitters at high redshift, (2) spatially-resolved spectroscopy for a large number of galaxies simultaneously, and (3) spectroscopic surveys without pre-imaging data (well suited for parallel programs).

Figure 5 shows the aXeSIM simulation of a 2-hour NIRCam LW grism exposure taken over the eXtreme Deep Field[30] (XDF) using the F356W filter. Here, the redshifts of all the sources have been set to 6 artificially to illustrate the detectability of Hβ and [O III] 4959/5007 Å lines as function of source brightness. In this image, the continuum is visible down to ~ 24 AB mag (~ 1 μJy) while emission lines are visible down to $\sim 2 \times 10^{-18}$ erg cm^{-2} s^{-1}. Although the confirmation of actual sensitivities has to wait for in-orbit observations, this simulation clearly demonstrates that NIRCam LW grism observations of extragalactic fields will produce rich data sets.

Recent studies indicate that the rest-frame optical emission lines of some $z \sim 7$ galaxies are quite luminous and have large equivalent widths.[31] The combined rest-frame equivalent width of Hβ+[O III] 4959/5007 Å lines can be well over 1000 Å, and could reach as high as 2000–3000 Å in some cases (e.g., Smit et al. 2014). This suggests that although the NIRCam LW grism mode is not as sensitive as NIRSpec, it may be quite effective in finding high-redshift galaxies through blind search for strong line emitters (note the high signal-to-noise emission lines in Fig. 5).

5.2 Wide-field Slitless Spectroscopy of Dark Clouds

Sun-like stars form in nearby dark clouds within our galaxy; the gas and dust within these regions is pulled together by gravity until the central regions form stars. These gravitationally-confined dark globules are very dense and emit no visible light, but they can be studied using the infrared

Fig 5 Left: *HST*/WFC3-IR F160W image of the Hubble eXtreme Deep Field[30] (XDF) covering the area around the Hubble Ultra-Deep Field (HUDF). The total exposure time is ~65 hours over most of the image; Center: 2-hour JWST NIRCam image in the F356W filter simulated with the source catalog produced from the XDF F160W image on the left. For simplicity, all the sources were assumed to be point-like (i.e., represented by the simulated WebbPSF F356W PSF) and $m_{356,AB} = m_{160,AB}$; Right: Simulated 2-hour NIRCam Module A R grism data with the F356W filter. The input model spectrum was constructed as a combination of a flat F_ν flux continuum and three emission lines, Hβ and [O III] 4959/5007 Å lines, with rest-frame equivalent widths of ~180, 200, and 600 Å, respectively (the line widths are unresolved). All sources were redshifted to $z = 6$ to illustrate the detectability of the three emission lines as function of source brightness. The images are oriented with North up and East to the left, and wavelength increases to the right (as in Fig. 4 with V3 PA = 0 deg.)

light of background stars.[32,33] The amount of dust (silicate and carbon grains) and gas material in these clumps can be measured by observing the brightness of these background stars at several different infrared wavelengths using NIRCam filter imaging.

These dark molecular clouds shield the dust particles inside of them from high energy ultraviolet radiation of the interstellar radiation field. Under these shielded conditions, the gas in the clouds can freeze out on dust grains and form mantles of ice. These ice mantles bring thousands of atoms and molecules into close proximity and are therefore the site of chemical reactions that begin to form more complex molecules such as H_2O, CO, CO_2, and H_3COH. Complex organic molecules can then form from these simple ones.[34]

The amount of H_2O, CO, CO_2, and perhaps other ice on a cloud's dust grains can be measured with NIRCam LW grism spectra, as simulated using aXeSIM for the B335 cloud in Figure 6. Background stars in high extinction regions of B335 show little overlap in their relatively short spectra through F430M (CO_2) or F460M (CO) filters, and most overlaps can be resolved with additional observations taken with the grism having dispersion in the perpendicular direction. Observations like these will show how the density of star-forming clouds changes with location and how volatile materials freeze out onto dust grains in the dense parts of clouds that may eventually form stars and planetary systems.

5.3 Spectra of Transiting Planets

We have used our 1-D spectral time-series simulator to model the expected JWST spectra of several transiting planets and estimate their scientific information content.[28] The simulated LW grism
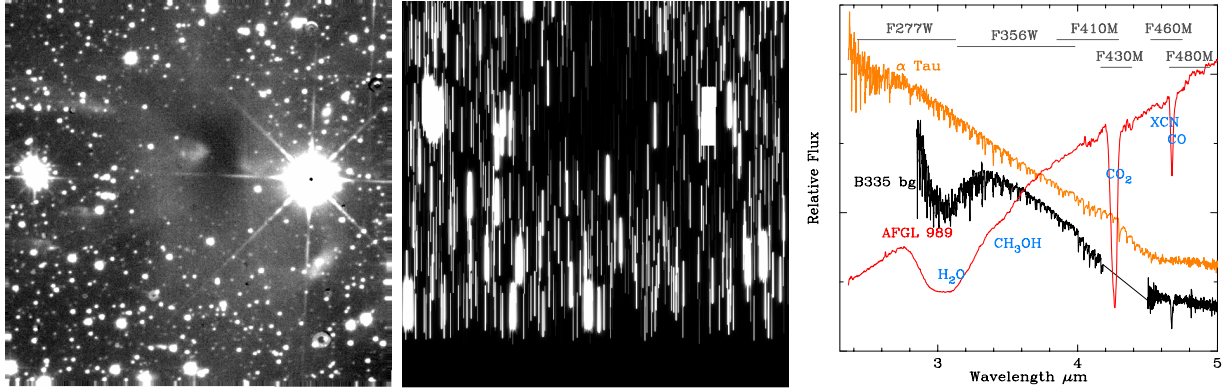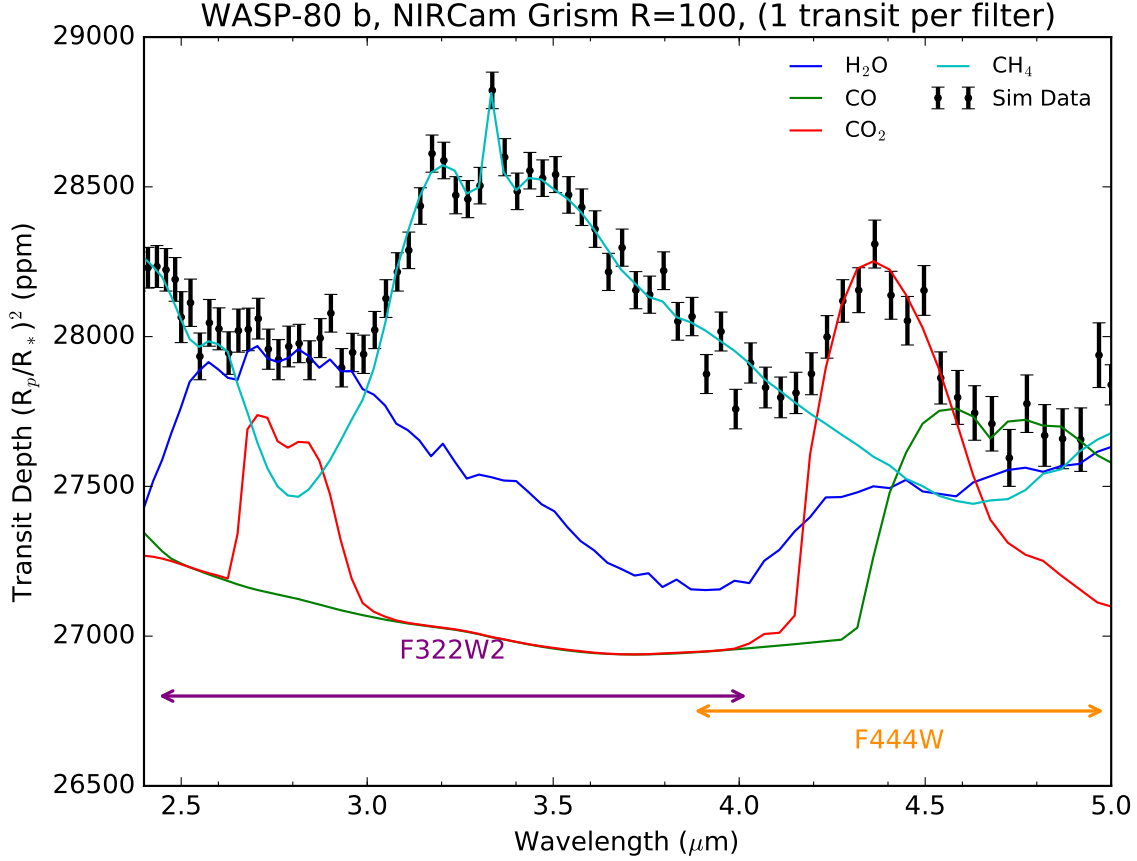
Fig 6 Left: B335 dark coud K-band ($\lambda = 2.2 \ \mu$m) UKIRT image acquired in 3.2 h integration time. Center: Simulated 0.45 h JWST NIRCam spectral image using the Module A C grism and F430M filter, using simulated PSFs for K = 20 mag (Vega) and brighter stars in the UKIRT data, and fainter stars added using the TRILEGAL background model[35] with measured extinctions applied. Spectra are vertically offset from the UKIRT image because the $\lambda = 4.0 \ \mu$m undeviated wavelength is outside of the bandpass of the F430M filter. Right: Interstellar ice spectra are shown with NIRCam filter bandpasses. A star behind the B335 cloud (black) is the same spectral type as α Tau[36] (orange), but it shows $\lambda = 3 \ \mu$m H_2O and CO ice absorption due to the intervening B335 cloud. The Infrared Space Observatory spectrum of AFGL 989[37] shows numerous strong and weak ice features that NIRCam will detect and measure, including $\lambda = 4.3 \ \mu$m CO_2 absorptions from ice mantles forming on dust grains in the cloud.

transmission spectra of WASP-80 b[38] is shown in Fig. 7. The spectral contributions of its major atmospheric constituents were modeled with CHIMERA[39,40] and are shown as solid colored curves, with the composite model spectrum being the highest value (largest absorption) at each wavelength. We binned the simulated observations of this model planet to spectroscopic resolving power R = 100 and show these points as black data points with error bars indicating their uncertainties. These observations would have to be made during two separate transits: one transit with a grism plus F322W2 filter and one with a grism and the F444W filter. SW observations can be made simultaneously with the LW grism exposures (see Sec. 4). This figure shows that NIRCam grism spectra are sensitive to strong CO (carbon monoxide) and CO_2 (carbon dioxide) features in hot planets $T > 1000$ K as well as CH_4 (methane) which is seen in cool planets $T \leq 1000$ K and also water (H_2O) which is ubiquitous in many planets. When combined with data at shorter wavelengths, these observations should constrain the metallicities, H_2O, CH_4, and CO mixing fractions of similar transiting planets to a factors of $\sim$5, much better than any current observations or shorter wavelength $JWST$ data alone.[28]

6 Observation Planning

The information provided above should be sufficient for assessing the basic feasibility of most NIRCam slitless spectroscopic observations. The Space Telescope Science Institute (STScI), the JWST science operations center, has developed detailed planning tools for determining integration times and designing observation sequences.

The new (as of 2017) $JWST$ ETC tool[27] incorporates all NIRCam modes supported for Cycle 1 observations, including wide-field and time series spectroscopy with the LW grisms. The user

13

Fig 7 Simulated transmission spectrum (black points with error bars) for the gas giant planet WASP-80 b[38] when observing with a NIRCam LWA grism paired with the F322W2 filter for one transit and with the F444W filter for one other transit, binned to $R = 100$. We model the planet's spectrum with CHIMERA[39,40] assuming a uniform temperature of 810 K, 7.5 times solar metallicity, and molecular mixing ratios consistent with chemical equilibrium. The figure shows the contributions of H_2O (water), CO (carbon monoxide), CO_2 (carbon dioxide), and CH_4 (methane) to the spectrum. The NIRCam grism modes are especially sensitive to the carbon-bearing molecules. The wavelength coverages of each individual transit for the F322W2 and F444W filters are also shown near the bottom of the plot.

generates a scene of sources and specifies observing parameters, and then ETC calculates signal-to-noise and other parameters. As described in Sec. 5, we can also provide NIRCam-specific configuration files for the aXeSIM package that can be used to simulate NIRCam LW grism observations and estimate their signal-to-noise. The PandExo[29] tool uses the Pandeia engine of the $JWST$ ETC to create observation simulations of all supported $JWST$ time-series spectroscopy modes, including the NIRCam LW grisms. Once the needed integration time has been calculated (e.g., from the ETC, aXeSIM, PandExo, or Tables 2 and 3), observation details can be planned with the Astronomer's Proposal Tool (APT) for JWST.[41] Current (version 25.0.5) and later versions of APT include templates for LW grism wide-field and single-object time-series observing modes. These templates allow selection of targets, detector readout (and subarray) parameters, filters, grisms, and (for the wide-field mode) mosaics and dithers. APT provides estimates of observing visibility windows for targets (consistent with the nominal launch date, orbit, and field of regard restrictions), as well as observing overheads.

Disclosures

The authors have no relevant financial interests in the manuscript and no other potential conflicts of interest.

Acknowledgments

References

1 C. A. Beichman, M. Rieke, D. Eisenstein, *et al.*, "Science opportunities with the near-IR camera (NIRCam) on the James Webb Space Telescope (JWST)," in *Space Telescopes and Instrumentation 2012: Optical, Infrared, and Millimeter Wave*, *Proceedings of the SPIE* **8442**, 84422N (2012).

2 J. E. Krist, C. A. Beichman, J. T. Trauger, *et al.*, "Hunting planets and observing disks with the JWST NIRCam coronagraph," in *Techniques and Instrumentation for Detection of Exoplanets III*, *Proceedings of the SPIE* **6693**, 66930H (2007).

3 M. J. Rieke, D. Kelly, and S. Horner, "Overview of James Webb Space Telescope and NIRCam's Role," in *Cryogenic Optical Systems and Instruments XI*, J. B. Heaney and L. G. Burriesci, Eds., *Proceedings of the SPIE* **5904**, 1–8 (2005).

4 T. Greene, C. Beichman, D. Eisenstein, *et al.*, "Observing exoplanets with the JWST NIRCam grisms," in *Techniques and Instrumentation for Detection of Exoplanets III*, *Proceedings of the SPIE* **6693**, 66930G (2007).

5 T. P. Greene, L. Chu, E. Egami, *et al.*, "Slitless spectroscopy with the James Webb Space Telescope Near-Infrared Camera (JWST NIRCam)," in *Society of Photo-Optical Instrumentation Engineers (SPIE) Conference Series*, *Proceedings of the SPIE* **9904**, 99040E (2016).

6 D. T. Jaffe, W. Wang, J. P. Marsh, *et al.*, "Fabrication and test of silicon grisms for JWST-NIRCam," in *Space Telescopes and Instrumentation 2008: Optical, Infrared, and Millimeter*, *Proceedings of the SPIE* **7010**, 70103L (2008).

7 F. Shi, B. M. King, N. Sigrist, *et al.*, "NIRCam Long Wavelength Channel grisms as the Dispersed Fringe Sensor for JWST segment mirror coarse phasing," in *Space Telescopes and Instrumentation 2008: Optical, Infrared, and Millimeter*, *Proceedings of the SPIE* **7010**, 70102E (2008).

8 E. Schlawin, M. Rieke, J. Leisenring, *et al.*, "Two NIRCam Channels are Better than One: How JWST Can Do More Science with NIRCam's Short-wavelength Dispersed Hartmann Sensor," *Publications of the Astronomical Society of the Pacific* **129**, 015001 (2017).

9 F. Shi, D. C. Redding, A. E. Lowman, *et al.*, "Segmented mirror coarse phasing with a dispersed fringe sensor: experiments on NGST's Wavefront Control Testbed," in *IR Space Telescopes and Instruments*, J. C. Mather, Ed., *Proceedings of the SPIE* **4850**, 318–328 (2003).

10 L. W. Huff, "NIRCam instrument optics," in *Cryogenic Optical Systems and Instruments XI*, J. B. Heaney and L. G. Burriesci, Eds., *Proceedings of the SPIE* **5904**, 30–37 (2005).

11 F. Shi, "Determine the DFS minimum detectable piston by measuring fringe tilt." unpublished.

12 F. Shi, "Preliminary Design of JWSTs Backup DFS in NIRCam Long Wavelength Channel October 26 Update." unpublished.

13 D. J. Schroeder, *Astronomical optics*, San Diego, Academic Press, second ed. (2000).

14 J. T. Rayner, "Evaluation of a solid KRS-5 grism for infrared astronomy," *Infrared Astronomical Instrumentation* **3354**(1), 289–294, SPIE (1998).

15 J. L. Barth, I. J. C., and C. Poivey, "The Radiation Environment for the Next Generation Space Telescope." [https://bhi.gsfc.nasa.gov/documents/Mission_Concept_Work/ISAL_January_2002_SST/SST_ISAL-1/Super_Star_Tracker/ngst_rad_env2.pdf] (2000). Accessed 19 May 2017.

16 B. J. Frey, D. B. Leviton, and T. J. Madison, "Temperature-dependent refractive index of silicon and germanium," in *Society of Photo-Optical Instrumentation Engineers (SPIE) Conference Series*, *Proceedings of the SPIE* **6273**, 62732J (2006).

17 J. Schubert, D. Lemke, W. Kraetschmer, *et al.*, "Alpha-radiation tests on the transmission of cryogenically cooled infrared filter materials used in ISOPHOT," in *Infrared Spaceborne Remote Sensing III*, M. S. Scholl and B. F. Andresen, Eds., *Proceedings of the SPIE* **2553**, 288–293 (1995).

18 "NIRCam Filters." [https://bhi.gsfc.nasa.gov/documents/Mission_Concept_Work/ISAL_January_2002_SST/SST_ISAL-1/Super_Star_Tracker/ngst_rad_env2.pdf]. Accessed 19 May 2017.

19 E. F. Erickson and D. Rabanus, "Beam shape effects on grating spectrometer resolution," *Applied Optics* **39**, 4486–4489 (2000).

20 "NIRSpec Overview." [https://jwst-docs.stsci.edu/display/JTI/NIRSpec+Overview]. Accessed 19 May 2017.

21 B. J. Rauscher, O. Fox, P. Ferruit, *et al.*, "Detectors for the James Webb Space Telescope Near-Infrared Spectrograph. I. Readout Mode, Noise Model, and Calibration Considerations," *"Publications of the Astronomical Society of the Pacific"* **119**, 768–786 (2007).

22 C. Beichman, B. Benneke, H. Knutson, *et al.*, "Observations of Transiting Exoplanets with the James Webb Space Telescope (JWST)," *Publications of the Astronomical Society of the Pacific* **126**, 1134–1173 (2014).

23 "NIRCam Detector Readout Patterns." [https://jwst-docs.stsci.edu/display/JTI/NIRCam+Detector+Readout+Patterns]. Accessed 19 May 2017.

24 "The Slitless Simulation package aXeSIM." [http://axe.stsci.edu/axesim/]. Accessed 19 May 2017.

25 M. Kümmel, J. R. Walsh, N. Pirzkal, *et al.*, "The Slitless Spectroscopy Data Extraction Software aXe," *Publications of the Astronomical Society of the Pacific* **121**, 59–72 (2009).

26 J. Leisenring, "pyNRC - A JWST NIRCam ETC." [https://github.com/JarronL/pynrc]. Accessed 19 May 2017.

27 "Welcome to the JWST Exposure Time Calculator." [https://jwst.etc.stsci.edu/]. Accessed 19 May 2017.

28 T. P. Greene, M. R. Line, C. Montero, *et al.*, "Characterizing Transiting Exoplanet Atmospheres with JWST," *The Astrophysical Journal* **817**, 17 (2016).

29 N. E. Batalha, A. Mandell, K. Pontoppidan, *et al.*, "PandExo: A Community Tool for Transiting Exoplanet Science with JWST & HST," *Accepted by Publications of the Astronomical Society of the Pacific* (2017).

30 G. D. Illingworth, D. Magee, P. A. Oesch, *et al.*, "The HST eXtreme Deep Field (XDF): Combining All ACS and WFC3/IR Data on the HUDF Region into the Deepest Field Ever," *The Astrophysical Journal Supplement* **209**, 6 (2013).

31 R. Smit, R. J. Bouwens, I. Labbé, *et al.*, "Evidence for Ubiquitous High-equivalent-width Nebular Emission in z ~ 7 Galaxies: Toward a Clean Measurement of the Specific Star-formation Rate Using a Sample of Bright, Magnified Galaxies," *The Astrophysical Journal* **784**, 58 (2014).

32 C. J. Lada, E. A. Lada, D. P. Clemens, *et al.*, "Dust extinction and molecular gas in the dark cloud IC 5146," *The Astrophysical Journal* **429**, 694–709 (1994).

33 C. J. Lada, J. F. Alves, and M. Lombardi, "Near-Infrared Extinction and Molecular Cloud Structure," *Protostars and Planets V* , 3–15 (2007).

34 A. C. A. Boogert, P. A. Gerakines, and D. C. B. Whittet, "Observations of the icy universe.," *Annual Review of Astronomy and Astrophysics* **53**, 541–581 (2015).

35 L. Girardi, M. A. T. Groenewegen, E. Hatziminaoglou, *et al.*, "Star counts in the Galaxy. Simulating from very deep to very shallow photometric surveys with the TRILEGAL code," *Astronomy & Astrophysics* **436**, 895–915 (2005).

36 L. Decin, C. Waelkens, K. Eriksson, *et al.*, "ISO-SWS calibration and the accurate modelling of cool-star atmospheres. I. Method," *Astronomy & Astrophysics* **364**, 137–156 (2000).

37 E. L. Gibb, D. C. B. Whittet, A. C. A. Boogert, *et al.*, "Interstellar Ice: The Infrared Space Observatory Legacy," *The Astrophysical Journal Supplement* **151**, 35–73 (2004).

38 A. H. M. J. Triaud, D. R. Anderson, A. Collier Cameron, *et al.*, "WASP-80b: a gas giant transiting a cool dwarf," *Astronomy & Astrophysics* **551**, A80 (2013).

39 M. R. Line, A. S. Wolf, X. Zhang, *et al.*, "A Systematic Retrieval Analysis of Secondary Eclipse Spectra. I. A Comparison of Atmospheric Retrieval Techniques," *The Astrophysical Journal* **775**, 137 (2013).

40 M. R. Line, H. Knutson, A. S. Wolf, *et al.*, "A Systematic Retrieval Analysis of Secondary Eclipse Spectra. II. A Uniform Analysis of Nine Planets and their C to O Ratios," *The Astrophysical Journal* **783**, 70 (2014).

41 "Astronomer's Proposal Tool." [http://www.stsci.edu/hst/proposing/apt]. Accessed 19 May 2017.

Thomas Greene is an Astrophysicist at NASA's Ames Research Center in Mountain View, CA. He received his PhD in Astronomy from the University of Arizona in 1991 and held positions at the University of Hawaii Institute for Astronomy and the Lockheed Martin Advanced Technology Center before joining Ames in 1998. Dr. Greene is a co-investigator on the JWST NIRCam instrument, a member of the JWST Mid-infrared science team, and studies young stars and extrasolar planets.

Biographies and photographs of the other authors are not available.

List of Figures

5 Left: *HST*/WFC3-IR F160W image of the Hubble eXtreme Deep Field[30] (XDF) covering the area around the Hubble Ultra-Deep Field (HUDF). The total exposure time is ∼65 hours over most of the image; Center: 2-hour JWST NIRCam image in the F356W filter simulated with the source catalog produced from the XDF F160W image on the left. For simplicity, all the sources were assumed to be point-like (i.e., represented by the simulated WebbPSF F356W PSF) and $m_{356,AB} = m_{160,AB}$; Right: Simulated 2-hour NIRCam Module A R grism data with the F356W filter. The input model spectrum was constructed as a combination of a flat F_ν flux continuum and three emission lines, Hβ and [O III] 4959/5007 Å lines, with rest-frame equivalent widths of ∼180, 200, and 600 Å, respectively (the line widths are unresolved). All sources were redshifted to $z = 6$ to illustrate the detectability of the three emission lines as function of source brightness. The images are oriented with North up and East to the left, and wavelength increases to the right (as in Fig. 4 with V3 PA = 0 deg.)

6 Left: B335 dark coud K-band ($\lambda = 2.2$ μm) UKIRT image acquired in 3.2 h integration time. Center: Simulated 0.45 h JWST NIRCam spectral image using the Module A C grism and F430M filter, using simulated PSFs for K = 20 mag (Vega) and brighter stars in the UKIRT data, and fainter stars added using the TRILEGAL background model[35] with measured extinctions applied. Spectra are vertically offset from the UKIRT image because the $\lambda = 4.0$ μm undeviated wavelength is outside of the bandpass of the F430M filter. Right: Interstellar ice spectra are shown with NIRCam filter bandpasses. A star behind the B335 cloud (black) is the same spectral type as α Tau[36] (orange), but it shows $\lambda = 3$ μm H$_2$O and CO ice absorption due to the intervening B335 cloud. The Infrared Space Observatory spectrum of AFGL 989[37] shows numerous strong and weak ice features that NIRCam will detect and measure, including $\lambda = 4.3$ μm CO$_2$ absorptions from ice mantles forming on dust grains in the cloud.

7 Simulated transmission spectrum (black points with error bars) for the gas giant planet WASP-80 b[38] when observing with a NIRCam LWA grism paired with the F322W2 filter for one transit and with the F444W filter for one other transit, binned to $R = 100$. We model the planet's spectrum with CHIMERA[39,40] assuming a uniform temperature of 810 K, 7.5 times solar metallicity, and molecular mixing ratios consistent with chemical equilibrium. The figure shows the contributions of H$_2$O (water), CO (carbon monoxide), CO$_2$ (carbon dioxide), and CH$_4$ (methane) to the spectrum. The NIRCam grism modes are especially sensitive to the carbon-bearing molecules. The wavelength coverages of each individual transit for the F322W2 and F444W filters are also shown near the bottom of the plot.

List of Tables